



**The reductive supercritical hydrothermal process, a novel synthesis method for cobalt nanoparticles: synthesis and investigation on the reaction mechanism**

Journal:	<i>Dalton Transactions</i>
Manuscript ID:	DT-ART-03-2014-000666.R1
Article Type:	Paper
Date Submitted by the Author:	02-May-2014
Complete List of Authors:	Seong, Gimyeong; A New Industry Creation Hatchery Center, Adschiri, Tadafumi; WPI-Advanced Institute for Materials Research, Tohoku University, ; Institute of Multidisciplinary Research for Advance Materials, Tohoku University, ; A New Industry Creation Hatchery Center, Tohoku University,

## Abstract

Highly crystalline cobalt nanoparticles with low surface oxidation were synthesized by the reductive supercritical hydrothermal process in the temperature range from 340 to 420 °C. Under these reaction conditions, hydrogen generated from formic acid decomposition is maximally soluble in water, enabling the effective reduction of cobalt ions and cobalt oxide. The reaction mechanism was investigated from kinetic analysis on the formation of cobalt nanoparticles. This analysis assumed the first order irreversible reaction and two different types of shrinking core models (chemical reaction and inter-diffusion dominated). According to the proposed reaction mechanism, cobalt monoxide is probably formed at the early reaction stage, where insufficient H<sub>2</sub> is available, or under high temperature conditions. Moreover, cobalt monoxide influences the entire reaction rate. Thus, suppressing the formation and growth of cobalt monoxide is of primary importance in the optimal synthesis of cobalt nanoparticles by the reductive supercritical hydrothermal process.

## 1 Introduction

Metal nanoparticles possess superior physical and chemical properties that have been widely exploited in research and industry over the past few decades. In particular, cobalt nanoparticles provide an excellent catalyst for the Fischer–Tropsch reaction<sup>1</sup> and carbon nanotube synthesis<sup>2</sup> because of their unique performances and high specific surface area. Cobalt nanoparticles have also been considered as a state-of-the-art technology-intensive

computer storage device because of their high coercivity.<sup>3,4</sup> Furthermore, cobalt nanoparticles are applicable to electro-optical<sup>5,6</sup> and the electro-magnetic technologies.<sup>7,8</sup>

To date, cobalt nanoparticles have been synthesized by various methods. However, environmental aspects such as exposure to toxic metals and the excessive use of organic solvents have not been sufficiently considered.<sup>9-13</sup> Environmental impacts should be thoroughly investigated before applying these methods in industry, especially at mass production scales.<sup>14</sup>

To prevent environmental exposure to toxic metals and minimize the use of organic solvents, Adschiri's group<sup>15-18</sup> has been developing supercritical water technology with hydrogen to synthesize metal nanoparticles. Formic acid was used as a reducing agent for metal ions or metal oxides since formic acid decomposes and releases hydrogen under the supercritical water condition<sup>19,20</sup>. Supercritical water is mainly advantageous, because it induces a homogeneous phase reaction that maximizes the solubility of hydrogen in water.

Sue *et al.*<sup>15,16</sup> used this approach to synthesize nickel nanoparticles, and Arita *et al.*<sup>17</sup> synthesized various metal nanoparticles by calculating the required amount of hydrogen using Ellingham diagrams<sup>21</sup>. In the author's previous research, the fugacity of hydrogen at near/supercritical conditions was calculated from thermodynamic models.<sup>18</sup> However, several notable issues have been omitted in previous studies. In particular, the development of the reaction mechanism and the suppression of metal oxide formation, which is presumed to occur at the thermodynamic equilibrium state between metal and metal oxide, have been neglected. The second of these considerations is important because metal oxides interfere with the reduction reaction.

This study investigates, for the first time, the reaction mechanism of cobalt nanoparticle

synthesis by the reductive supercritical hydrothermal process. First, cobalt nanoparticles were synthesized under homogeneous phase conditions between 340 and 420 °C (sub-cooled liquid to supercritical water) for a specific reaction time. The concentration of formic acid appropriate to the reaction temperature was explored. Second, the formation of cobalt nanoparticles was subjected to kinetic analysis, assuming the first-order irreversible reaction and two shrinking core models.<sup>22-24</sup> Finally, based on the kinetic analysis, the most appropriate reaction mechanism was proposed, and the optimal synthesis conditions were identified.

## **2 Experimental section**

### **2.1 Materials**

Cobalt (II) acetate-tetra-hydrate, methanol, formic acid (98%) and cobalt standard solution (1000 mg/L) were purchased from Wako Pure Chemical Industries, Ltd., and they were used without further purification. Purified water was purchased from Daiwa Yakuhin and further purified through a membrane filter (MILLI PORE: 0.1 μm).

### **2.2 Experimental procedure**

Cobalt (II) acetate tetra-hydrate aqueous solution ( $1.00 \times 10^{-1}$  M) was prepared as a precursor and various concentrations of formic acid (up to 16.6 M) were used as reducing

agents. First, the precursor solution was loaded into the Ti–alloy batch-type reactors (inner volume = 5 ml). The volumes (in ml) of loaded solution were 3.23, 3.07, 2.85, 0.82, 0.61 and 0.52 at fixed temperatures (in °C) of 350, 365, 375, 400, 425 and 450, respectively. Based on the volume of the aqueous solution under all the temperature conditions, the presumed inner pressure was 22.1 MPa. Second, a specified volume of formic acid was loaded into the reactors and the reactors closed. To avoid exposure to air, each step was performed in Ar-filled glove box.

Third, the reactors were transferred from the glove box to an electric furnace where they were heated for 10 min at specified temperatures (for kinetic analysis, samples were heated for 1–120 min). The inner temperature (in °C) reached 340, 350, 360, 380, 400 and 420 within 3–5 min, at set temperatures (in °C) of 350, 365, 375, 400, 425 and 450, respectively. Hereafter, the stabilized inner temperature is called the reaction temperature.

Once the reaction was complete, the reactors were removed from the furnace and immediately immersed in a water bath at room temperature to quench the reaction. The quenched reactors were slightly opened to release the generated gases, closed again and returned to the glove box. Fourth, the caps of the reactors were completely removed and the products were collected by methanol addition to prevent further oxidation from contacting with water. The collected solution was removed from the glove box. The products were repeatedly (more than three times) washed with methanol by centrifugation and decantation. Finally, the products were vacuum-dried at room temperature in a desiccator.

To identify the entire reaction mechanism, cobalt monoxide was prepared for comparison with the original precursor, which was synthesized at 360 °C for 10 min under formic acid-free conditions. The synthesized cobalt monoxide was separated into two size groups by

precipitation in methanol for 2 h. The average sizes (diameter) of the size-selected cobalt monoxide were  $93 \pm 5$  and  $407 \pm 5$  nm, obtained by counting more than 300 particles from transmission electron microscope (TEM, Hitachi H7650, 100 kV) images of each group.

### 2.3 Characterization

The crystallographic phase of the product was investigated by powder X-ray diffraction (XRD, Rigaku Ultima IV apparatus with Cu K $\alpha$  radiation,  $\lambda = 0.154$  nm,  $2\theta = 20\text{--}80^\circ$  operated at 40 kV and 40 mA). The molar ratio between the cobalt and cobalt monoxide in the product was obtained by the internal standard technique.<sup>25</sup> The standard samples were selected from the cobalt and cobalt monoxide synthesized in the presence and absence of formic acid at 360 °C for 10 min. The XRD peak area intensity ratio,  $R_X$  is given by

$$R_X = \frac{\text{Co}((111,\text{fcc})+(002,\text{hcp}))}{\text{Co}((111,\text{fcc})+(002,\text{hcp}))+\text{CoO}(200,\text{fcc})} \quad (1)$$

where the values in the parentheses are the XRD peak area intensities of the particular crystal planes of cobalt or cobalt monoxide.

Figure 1 plots the standard curve of the molar ratio of cobalt in the standard samples ( $R_M$ ) versus the XRD peak area intensities ratio ( $R_X$ ). The relationship between  $R_M$  and  $R_X$  is given by the following correlation equation:

$$R_M = \frac{N_{\text{Co}}}{N_{\text{Co}}+N_{\text{CoO}}} = -0.521R_X^2 + 1.513R_X \quad (\text{standard deviation: } \pm 0.31) \quad (2)$$

where  $N_{\text{Co}}$  and  $N_{\text{CoO}}$  represent the number of moles of Co and CoO, respectively.

The size and morphology of the products, and their elemental makeup, was analyzed by energy-dispersive X-ray spectroscopy (EDS) installed scanning electron microscope (SEM,

JEOL JSM-6500F, 15 kV) and high-resolution transmission electron microscope (HR-TEM, Hitachi HF2000, 200 kV). To analyze the reaction conversion, the concentration of cobalt ions in the unreacted solution was measured by inductively coupled plasma atomic emission spectroscopy (ICP, SPECTRO ARCOS EOP).

### 3 Results and discussion

#### 3.1 Effect of molar concentration of formic acid

The effect of molar concentration of formic acid on cobalt nanoparticles formation was investigated under six isothermal conditions (340, 350, 360, 380, 400 and 420; all temperatures in °C). Each isothermal condition induces a homogeneous phase reaction that maximally solubilizes hydrogen in water.

Crystallographic phase changes in the product were investigated by XRD. Since the XRD peak patterns at different temperatures were very similar, a single representative result is shown in Fig. 2. This figure shows the XRD peak patterns of the products synthesized at 340 °C. The loaded concentration of formic acid gradually increases from (a) through (i). At low formic acid concentration (a–d), only the cobalt monoxide phase appears. At a formic acid concentration of 0.16 M (e), the cobalt phase appears for the first time. At sufficiently high formic acid concentrations, cobalt peaks alone are observed (g–i).

Sample (g) was subjected to further SEM, TEM and EDS analysis to determine the size, morphology and the surface oxidation state of the particles. For comparison, cobalt

nanoparticles synthesized under supercritical conditions (380 °C and formic acid: 7.3 M) were analyzed by the same methods. SEM imaging of sample (g) (Fig. 3 (a)) reveals aggregated and agglomerated particles. The particles are irregular and their size varies from hundreds of nanometers to several micrometers. Under none-modification condition, nanoparticles are easily aggregated and agglomerated since interaction between particles increases with increasing surface area. Figure 3 (b) shows the EDS spectrum of the sample imaged in Fig. 3 (a). Although strong cobalt peaks predominate, a relatively small oxygen peak is also observed. The oxygen peak indicates a possible oxidation layer, which could form on the particle surfaces to a thickness of several nanometers. This oxidation layer could establish during exposure to air after the reaction, hereafter referred to as secondary oxidation.

Figure 3 (c) shows an SEM image of the cobalt nanoparticles synthesized at 380 °C. Unlike Fig. 3 (a), the particles are small and spherical (diameter: 100–150 nm). Small cobalt particles could form by simultaneous fast nucleation and growth, probably originating from the enhanced degree of supersaturation at the supercritical point.<sup>26</sup> In the EDS spectrum of Fig. 3 (d), the small particle (indicated by the crosshair in Fig. 3(c)) is identified as cobalt nanoparticle for the above-described reasons. Interestingly, the core of the small particle remains in the metallic phase despite its miniscule size. Therefore, the oxidation layer can be inferred to prevent further oxidation of the particle.

Figure 3 (e) shows a high resolution TEM image of a part of the agglomerated particles in Figure 3 (c). The sizes of the agglomerated particles are approximately 20 nm. The inter-planer spacing lattice parameter (centre positioned particle) was obtained from the image and matched with (100) hcp cobalt crystallographic phase. On the surface of the

particles, amorphous layer is observed. This amorphous layer can be cobalt oxide or cobalt hydroxide layer formed by the secondary oxidation as mentioned above. Thus, both of EDS and HR-TEM data satisfy that those particles are metallic cobalt nanoparticles surrounded by amorphous oxide/hydroxide layer that can prevent further oxidation of the particles.

To understand how the crystallographic phase in the product alters with the reaction conditions, the molar ratio of metallic cobalt phase was quantified. The preparation of the standard samples and the calibration curve are detailed in the Experimental section. Figure 4 plots the molar ratio of the cobalt phase as a function of molar formic acid concentration at six different temperatures (340–420 °C). As the reaction temperature increased, higher concentration of formic acid was required to produce cobalt nanoparticles. This result can be explained as follows: As the reaction temperature increases, the reaction equilibrium is driven to the left in the following reaction, Eq. (3–4), since the reaction is exothermic.<sup>17,18,21</sup>



$$\frac{\text{M}}{\text{MO}} = K \frac{\text{H}_2}{\text{H}_2\text{O}} = \frac{\text{H}_2}{\text{H}_2\text{O}} \exp\left(-\frac{\Delta H}{RT}\right) \quad (4)$$

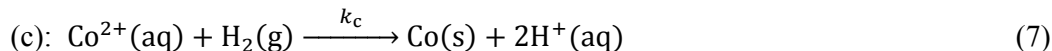
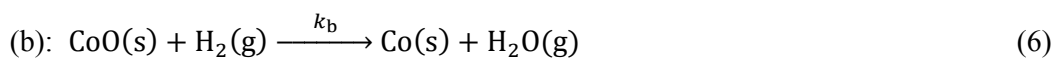
Here, M denotes a metal,  $K$  is the equilibrium constant of the reaction,  $\Delta H$  is the enthalpy change of the reaction and  $R$  is the universal gas constant.

The rise of the cobalt phase with increasing formic acid concentration also strongly depends on temperature. The crystallographic phase steeply rises from 340 to 360 °C and increases more gently at higher temperatures (380–420 °C). If this phenomenon was solely attributable to the exothermic reaction, the cobalt phase should linearly increase with formic acid (or  $\text{H}_2$ ) concentration, in accordance with Eq. (3)–(4). However, the increase rates are clearly nonlinear, especially in the higher temperature (380–420 °C). In this temperature range, sharp increases occur up to a molar ratio of 0.4, followed by gentler increases from 0.4

to 1.0. This phenomenon suggests multi-reaction pathways and steps in the reaction system. The possible reaction mechanism was investigated by kinetic analysis discussed next.

### 3.2 Kinetic approach to cobalt nanoparticle synthesis

Three chemical reactions are expected in the reaction system:



where  $k_a$ ,  $k_b$  and  $k_c$  are the reaction rate constants of reactions (a), (b) and (c), respectively.

When the hydrogen concentration is deficient as at lower formic acid concentrations or early reaction stages, or when formic acid is insufficiently converted to  $\text{H}_2$ , the predominant reaction is (a). Once formic acid is fully converted to  $\text{H}_2$ , reaction (b) can proceed. Hereafter, this reaction pathway is denoted path A. Conversely, if hydrogen concentration is sufficient at the outset, reaction (c) can proceed: this reaction pathway is called as path B.

To confirm whether these reaction schemes proceed in practice, the conversion of cobalt ions ( $1.00 \times 10^{-1}$  M) was investigated in detail at two reaction temperatures (380 and 400 °C), under formic acid-free and formic acid-injected conditions. The formic acid concentration was 1.37 M at both temperatures, sufficiently high to reduce cobalt oxide.<sup>18</sup> The conversion of cobalt ions,  $X_{\text{Co}^{2+}}$  versus the reaction time,  $t$  is plotted in Fig. 5 under four reaction conditions.

In Fig. 5, the conversion of cobalt ions follows a similar trend under all conditions. The conversions initially increase rapidly, and increase more slowly after 1200 s. However, these

conversion increases require more detailed examination, because the reaction pathways and steps clearly depend on the presence of formic acid. Under the formic acid-free condition, conversion increases rapidly up to  $X_{\text{Co}^{2+}} = 0.279$  and gradually increases thereafter (up to  $X_{\text{Co}^{2+}} = 0.480$ ). In addition, the conversions appear to have saturated at this conversion. This saturation phenomenon may be related to the solubility limit of CoO in water,<sup>27</sup> and is attributable to the reaction (a) alone. Thus, the reaction system under formic acid-free conditions can be assumed as a first-order reversible reaction of  $\text{Co}^{2+}$ .

To analytically solve the reaction system, we employ the following pseudo first-order irreversible reaction model:<sup>22</sup>

$$-\ln\left(1 - \frac{X_{\text{Co}^{2+}}}{X_{\text{eq}}}\right) = \frac{1}{X_{\text{eq}}} k_a t \quad (8)$$

$$K_a = \frac{X_{\text{eq}}}{1 - X_{\text{eq}}} = \frac{k_a}{k_r} \quad (9)$$

where  $X_{\text{eq}}$  is the conversion at equilibrium,  $K_a$  is the equilibrium constant of reaction (a) and  $k_r$  is the reaction rate constant of the inverse reaction (a). The equilibrium conversions,  $X_{\text{eq}}$ , estimated from Fig. 5 are 0.480 and 0.450 at 380 and 400 °C, respectively.

According to Eq. (8), the rate constant,  $k_a$  can be obtained from the slope of a  $-\ln(1 - X_{\text{Co}^{2+}}/X_{\text{eq}})$  versus  $t$ , which gives  $k_a / X_{\text{eq}}$ . Therefore,  $-\ln(1 - X_{\text{Co}^{2+}}/X_{\text{eq}})$  was plotted as a function of  $t$  under formic acid-free conditions at two reaction temperatures (Fig. 6). Linear regression analysis revealed strong linearity (linear regression coefficient  $R^2 = 0.981$  at 380 °C and 0.860 at 400 °C). The equilibrium constant,  $K_a$  and the rate constant,  $k_r$  were then calculated from Eq. (9). The values so obtained are tabulated in Table 1. Finally, the reaction conversion of  $\text{Co}^{2+}$  under the formic acid-free condition was fitted to Eq. (8) using the parameters listed in Table 1 (time interval = 10 s: Fig. 5). The calculated and experimental

results are in favorable agreement.

Similar trends in  $X_{\text{Co}^{2+}}$  are observed in the presence of formic acid. However, the reaction conversions increase to much higher values than when formic acid is absent ( $X_{\text{Co}^{2+}} = 0.523$ ), and thereafter gradually increase up to 0.884. Moreover, when cobalt ions were leached after attaining their maximum values, conversion decreased, indicating that cobalt nanoparticles were partially dissolved in acidic water (approximately pH 3.5). Therefore, the expected reaction pathways for cobalt nanoparticles formation are more complicated in the presence of formic acid than in its absence. Specially, (1) reactions (a) and (b) can proceed in series (path A) and (2) reactions (a) and (c) can proceed in parallel (path B).

To understand the above reaction pathway scheme, the product yields of Co and CoO as well as the reaction conversion of cobalt ions, were subjected to kinetic analysis. In Fig. 7, the reduction fraction of cobalt ions,  $f_{\text{Co}}$  (indicating the Co yield) is plotted as a function of reaction time,  $t$  at two reaction temperatures. For comparison, the fraction of CoO in the samples ( $f_{\text{CoO}}$ ) is also plotted. Here,  $f_{\text{Co}}$  and  $f_{\text{CoO}}$  are defined as follows:

$$f_{\text{Co}} \equiv \frac{N_{\text{Co}}}{N_{\text{Co}} + N_{\text{CoO}}} \times X_{\text{Co}^{2+}} \quad (10)$$

$$f_{\text{CoO}} \equiv \frac{N_{\text{CoO}}}{N_{\text{Co}} + N_{\text{CoO}}} \times X_{\text{Co}^{2+}} \quad (11)$$

where  $N_{\text{Co}}$  and  $N_{\text{CoO}}$  represent the number of moles of cobalt and cobalt monoxide, respectively. The selectivities of Co ( $\frac{N_{\text{Co}}}{N_{\text{Co}} + N_{\text{CoO}}}$ ) and CoO ( $\frac{N_{\text{CoO}}}{N_{\text{Co}} + N_{\text{CoO}}}$ ) can be obtained from Fig. 4, and the reaction conversion of cobalt ions  $X_{\text{Co}^{2+}}$  can be obtained from Fig. 5.

Early in the reaction, the reduction fraction was minimal, while the CoO fraction was high. This implies that CoO is the dominant initial product, but is gradually reduced to Co as the

reaction proceeded. At this stage, the reaction system is dominated by path A probably because  $H_2$  is deficient. In batch reactor, the rate of formic acid decomposition strongly depends on the temperature profiles of the solution in batch reactors.<sup>19,28,29</sup>

The reaction path A under formic acid-injected conditions can be analyzed from a reaction model in which heterogeneous reactions occur in series. However, an analytical or a numerical solution of the reaction pathway remains elusive. If reaction (b) occurs once reaction (a) is complete, the entire system can be analyzed using different kinetic models, since reaction (a) should proceed much more rapidly than reaction (b).

First, reaction (a) can be expressed as a first-order irreversible reaction if the reaction proceeds in two stages: (1)  $H_2$  deficiency (exemplified by 0–1200 s at 380 °C and 0–900 s at 400 °C) and (2)  $H_2$  sufficiency (occurring after 1200 s at 380 °C and after 900 s at 400 °C). Thus, the reaction rate constants  $k_a^f$  (where the superscript f indicates injected formic acid) can be obtained from the slopes of  $-\ln(1 - X_{Co^{2+}})$  versus  $t$  plots, as shown in Fig. 8. The obtained reaction rate constants are tabulated in Table 2, and the calculated results are plotted in Fig. 5 (time interval = 10 s). Again, the calculated results satisfactorily agree with the experimental data.

The size of the intermediate CoO is an important indicator of the rate constant of reaction (b),  $k_b$ , since the reduction occurs on the CoO surface. However, the size of CoO particles is difficult to measure during the reaction. Therefore, to investigate the rate constant of reaction (b), similar reaction systems (starting from 0.082 mmol CoO in 0.82 ml  $H_2O$  and 1.37 M HCOOH) were prepared at 380 and 400 °C, the CoO particles were separated by size (average diameter  $d = 93 \pm 5$  and  $407 \pm 5$  nm) and the reduction fractions were compared to those of the original precursor.

Figure 9 plots the reduction fraction of CoO,  $f_{\text{Co}}^{\text{s}}$  ( $\equiv N_{\text{Co}}/(N_{\text{Co}} + N_{\text{CoO}})$ , where the superscript s represents solid) at two reaction temperatures. The reduction fraction of Co ions  $f_{\text{Co}}$  is also plotted for comparison (from Fig. 7). In the case of 93 nm-sized CoO particles, the reduction fraction sharply increased after 900 s (to 0.286) and 1200 s (to 0.442) at 380 °C and 400 °C, respectively. By contrast, the reduction fraction obtained in the original precursor system (0.877 and 0.819 at 380 and 400 °C, respectively) was much higher indicating that the CoO particles formed during the reduction of the original precursor were much smaller than 93 nm. Conversely, no reduction occurred on 407 nm-sized CoO particles, despite reaction temperature, further implicating size as an important factor of CoO reduction.

The reduction of CoO and the original precursor was further analyzed by a shrinking core model. Since all reduction fractions in Fig. 9 exhibit sharp increase followed by gradual increase, two different reaction stages may occur together: (1) a reaction stage controlled by chemical reaction and (2) a reaction stage controlled by inter-diffusion. Assuming that CoO particles are spherical and that reduction is dominated by the chemical reaction occurring at the interface between the product layer and the unreacted core of each small particle, the chemical reaction controlled shrinking core model can be applied to the system as follows:<sup>23,24</sup>

$$\frac{t}{\tau} = 1 - (1 - f)^{1/3} \quad (12)$$

$$\tau = \frac{\rho_{\text{CoO}} r_{\text{ini}}}{k C_{\text{H}_2}} \quad (13)$$

where  $t$  is the reaction time,  $f$  is the reduction fraction of CoO (here,  $f_{\text{Co}}$  or  $f_{\text{Co}}^{\text{s}}$ ),  $r_{\text{ini}}$  is the initial radius of the CoO particles,  $\rho_{\text{CoO}}$  is the density of CoO (6.44 g/cm<sup>3</sup>),  $C_{\text{H}_2}$  is the molar concentration of H<sub>2</sub> and  $k$  is the first-order rate constant of the surface reaction. Here,  $C_{\text{H}_2}$

can be replaced by the molar concentration of formic acid,  $C_{\text{HCOOH}}$ . The inter-diffusion controlled shrinking core model is represented by<sup>23,24</sup>

$$\frac{t}{\tau} = 1 - 3(1 - f)^{2/3} + 2(1 - f) \quad (14)$$

$$\tau = \frac{\rho_{\text{CoO}} r_{\text{ini}}^2}{6D_e C_{\text{H}_2}} \quad (15)$$

where  $D_e$  is the effective diffusion coefficient of gaseous reactants in the ash layer. Hence,  $k$  and  $D_e$  can be obtained by plotting  $1 - (1 - f)^{1/3}$  and  $1 - 3(1 - f)^{2/3} + 2(1 - f)$ , respectively, as functions of  $t$  and determining the respective slopes.

During the early reaction stage, the chemical controlled reaction model was applied to the 93 nm-sized CoO particles and the original precursor. Figure 10 (a) shows the plots of  $1 - (1 - f)^{1/3}$  against  $t$  under four reaction conditions. The slopes of the plots were determined by linear regression, and  $k_b$  was determined from Eq. (13). The inter-diffusion controlled reaction model was applied to later reaction stages. Under the same conditions,  $1 - 3(1 - f)^{2/3} + 2(1 - f)$  is plotted against  $t$  in Fig. 10 (b). Here, only the original precursor was analyzed because the reaction of 93 nm-sized CoO particles was assumed to stop before 3600 s. All of the plots for each model are sufficiently linear to validate the analysis. The obtained values are tabulated in Table 3. The original precursor yields only  $\tau^{-1}$  because the CoO radius at the initial stage is unknown, as mentioned above. Finally, the reduction fractions,  $f_{\text{Co}}$  and  $f_{\text{Co}}^{\text{S}}$  were fitted to Eq. (12) and Eq. (14), respectively, using the parameters listed in Table 3, and the calculated results are plotted in Fig. 9.

The calculated results obtained from both shrinking core models are consistent with the experimental results. The reaction rate in the original precursor system is lower at 380 °C than at 400 °C in the chemical reaction controlled stage. However, the reaction rate at 380 °C

far exceeds that at 400 °C in the inter-diffusion controlled stage. This phenomenon may be related to the size of CoO particles. When the CoO particles are large, the chemical reaction proceeds rapidly, since the available CoO surface area is large. Conversely, the inter-diffusion reaction is slowed by the increased distance between the core and the H<sub>2</sub> source. This suggests that the CoO crystals are smaller at 380 °C than at 400 °C. CoO crystals of similar size (93 nm) yielded similar reaction rate constants.

### 3.3 Reaction mechanism

Combining the results of the previous sections, the cobalt nanoparticles are proposed to form by the following mechanism (schematized in Fig. 11). First, cobalt acetate tetra-hydrate is ionized to cobalt cation and acetate anion in aqueous solution. Subsequently, cobalt nanoparticles can be synthesized via two reaction pathways, path A and path B, which may simultaneously occur in the presence of formic acid. Since the reaction pathways strongly depend on the degree of formic acid decomposition, path A dominates in the investigated temperature range. Subsequently to reaction completion, the cobalt nanoparticle surfaces can be partially oxidized by atmospheric exposure (secondary oxidation) or partially dissolved in the acidic condition, especially at high formic acid concentrations. In the absence of formic acid, reaction (a) and the inverse of reaction (a) occur.

The experimental data and the derived reaction mechanism suggest that cobalt monoxide is probably formed under conditions of insufficient H<sub>2</sub> or high temperature. Cobalt monoxide can partially determine the main reaction pathway as well as the rate of reaction (b), indicating that the entire reaction rate depends on the size of the cobalt monoxide particles.

Therefore, suppressing the formation and growth of cobalt monoxide is primarily important for optimizing the synthesis conditions of cobalt nanoparticles in this reaction system.

## 4 Conclusions

Cobalt nanoparticles were successfully synthesized by the reductive supercritical hydrothermal process. In this method, the homogeneous reaction conditions enable maximum solubility of hydrogen in water. The produced cobalt nanoparticles were highly crystalline and exhibited little surface oxidation. Moreover, the probable reaction mechanism of cobalt nanoparticle formation was identified from kinetic analysis models. The main reaction pathway proceeds via two tandem reactions: the early stage formation and later stage reduction of cobalt monoxide. Since cobalt monoxide, which influences the entire reaction rate, is probably formed at the early reaction stage or at high temperatures, its formation and growth should be suppressed during the optimal synthesis of cobalt nanoparticles by the reductive supercritical hydrothermal process.

## Acknowledgements

This research was supported by New Energy and Industrial Technology Development Organization Japan (NEDO), the Ministry of Education, Science, Sports and Culture of Japan (083042, MEXT) and Japan Science and Technology Agency (JST-CREST). The SEM

images with EDS spectra and HR-TEM images were supported by Mr. Miyazaki at Integrated analysis room, and ICP data were supported by Mr. Akiyama at technical room in Tohoku University. The authors would like to thank Enago ([www.Enago.jp](http://www.Enago.jp)) for the English language review.

## References

- 1 J. P. den Breejen, P. B. Radstake, G. L. Bezemer, J. H. Bitter, V. Frøseth, A. Holmen and K. P. de Jong, *J. Am. Chem. Soc.*, 2009, **131**, 7197–7203.
- 2 U. Narkiewicz, M. Podsiadły, R. Jędrzejewski and I. Pelech, *Appl. Catal. A*, 2010, **384**, 27–35.
- 3 T. N. Narayanan, M. M. Shaijumon, P. M. Ajayan and M. R. Anantharaman, *J. Phys. Chem. C*, 2008, **112**, 14281–14285.
- 4 Y. Soumare, C. Garcia, T. Maurer, G. Chaboussant, F. Ott, F. Fievet, J. Y. Piquemal and G. Viau, *Adv. Funct. Mater.*, 2009, **19**, 1971–1977.
- 5 A. Horikawa, K. Yamaguchi, M. Inoue, T. Fujii and K. I. Arai, *Mater. Sci. Eng. A*, 1996, **217/218**, 348–352.
- 6 M. Levy, A. A. Jalali and X. Huang, *J. Mater. Sci: Mater. Electron*, 2009, **20**, S43–47.
- 7 Y. Yang, C. L. Xu, L. Qiao, X. H. Li and F.S. Li, *Chin. Phys. Lett.*, 2010, **27**, 057501.
- 8 P. Gambardella, S. Rusponi, M. Veronese, S. S. Dhesi, C. Grazioli, A. Dallmeyer, I. Cabria, R. Zeller, P. H. Dederichs, K. Kern, C. Carbone and H. Brune, *Science*, 2003, **300**, 1130–1133.
- 9 H. D. Jang, D. W. Hwang, D. P. Kim, H. C. Kim, B. Y. Lee and I. B. Jeong, *Mater. Res.*

- Bull.*, 2004, **39**, 63–70.
- 10 R. N. Grass and W. J. Stark, *J. Mater. Chem.*, 2006, **16**, 1825–1830.
- 11 V. F. Puentes, D. Zanchet, C. K. Erdonmez and A. P. Alivisatos, *J. Am. Chem. Soc.*, 2002, **124**, 12874–12880.
- 12 H. Yang, T. Ogawa, D. Hasegawa, C. N. Chinnasamy and M. Takahashi, *J. Magn. Magn. Mater.*, 2006, **304**, e10–e12.
- 13 A. Kumbhar, L. Spinu, F. Agnoli, K-Y. Wang, W. Zhou and C. J. O'Connor, *IEEE Trans. Magn.*, 2001, **37**, 2216–2218.
- 14 R. A. Sheldon, *Green Chem.*, 2005, **7**, 267–278.
- 15 K. Sue, A. Suzuki, M. Suzuki, K. Arai, Y. Hakuta, H. Hayashi and T. Hiaki, *Ind. Eng. Chem. Res.*, 2006, **45**, 623–626.
- 16 K. Sue, A. Suzuki, M. Suzuki, K. Arai, T. Ohashi, K. Matsui, Y. Hakuta, H. Hayashi and T. Hiaki, *Chem. Lett.*, 2006, **35**, 960–961.
- 17 T. Arita, H. Hitaka, K. Minami, T. Naka and T. Adschiri, *J. Supercrit. Fluids*, 2011, **57**, 183–189.
- 18 G. Seong, S. Takami, T. Arita, K. Minami, D. Hojo, A. R. Yavari and T. Adschiri, *J. Supercrit. Fluids*, 2011, **60**, 113–120.
- 19 J. Yu and P. E. Savage, *Ind. Eng. Chem. Res.*, 1998, **37**, 2–10.
- 20 T. Yagasaki, S. Saito and I. Ohmine, *J. Chem. Phys.*, 2002, **117**, 7631–7639.
- 21 H. J. T. Ellingham, *J. Soc. Chem. Ind.*, 1944, **63**, 125.
- 22 O. Levenspiel, *Chemical reaction engineering*, John Wiley & Sons, Inc. New York, 3rd edn., 1999, Ch. 3, pp. 41–57.
- 23 O. Levenspiel, *Chemical reaction engineering*, John Wiley & Sons, Inc. New York, 3rd

end., 1999, Ch. 25, pp. 575–579.

- 24 J. A. Bustnes, D. Sichen and S. Seetharaman, *Metall. Mater. Trans. B*, 1995, **26B**, 547–552.
- 25 B. D. Cullity and S. R. Stock, *Elements of X-ray diffraction*, Addison-Wesley Publishing Co. Inc., 3rd edn., 2001, Ch. 14, pp. 388–400.
- 26 T. Adschiri, Y. Hakuta, K. Sue and K. Arai, *J. Nanopart. Res.*, 2001, **3**, 227–235.
- 27 M-T. Liang, S-M. Chern, C-Y. Hsu, Q-F. Li, N-J. Ye, H-Y. Lu and Z-J. Chung, The solubility of cobaltous salts in supercritical water, Proceedings of the 6<sup>th</sup> International Symposium on Supercritical Fluids (ISASF), Versailles, France, 2003.
- 28 N. Akiya and P. E. Savage, *AIChE J.*, 1998, **44**, 405–415.
- 29 T. Sato, S. Kurosawa, R. L. Smith Jr., T. Adschiri and K. Arai, *J. Supercrit. Fluids*, 2004, **29**, 113–119.

**Table 1** Parameters of the pseudo first-irreversible reaction model in the absence of formic acid

$T$ (°C)	$k_a/X_{\text{eq}}$ ( $\text{s}^{-1}$ )	$K_a$	$k_a$ ( $\text{s}^{-1}$ )	$k_r$ ( $\text{s}^{-1}$ )
380	$7.61 \times 10^{-4}$	0.923	$3.65 \times 10^{-4}$	$3.96 \times 10^{-4}$
400	$7.53 \times 10^{-4}$	0.818	$3.39 \times 10^{-4}$	$4.14 \times 10^{-4}$

**Table 2** Reaction rate constants of the two-stage reaction in the presence of formic acid, obtained by linear regression of the  $-\ln(1 - X_{\text{CO}_2^+})$  versus reaction time plot

$T$ (°C)	$k_a^f$ (s <sup>-1</sup> )	
	Stage (1)	Stage (2)
380	$7.41 \times 10^{-4}$	$2.70 \times 10^{-4}$
	<sup>a</sup> (0.840)	(0.971)
400	$1.10 \times 10^{-3}$	$2.03 \times 10^{-4}$
	(0.857)	(0.956)

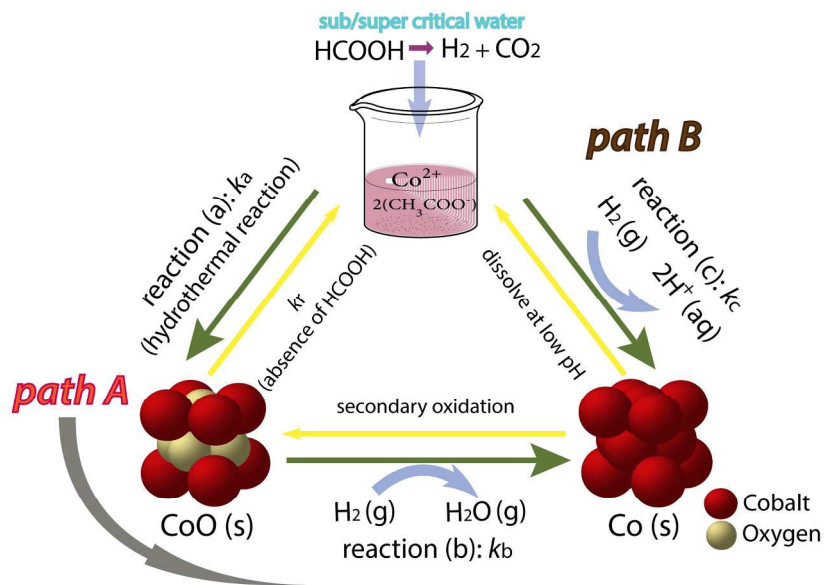
<sup>a</sup> linear regression coefficient,  $R^2$

**Table 3** Parameters of the chemical reaction controlled and the inter-diffusion controlled shrinking core models

		380 °C		400 °C	
		CoO	Original precursor	CoO	Original precursor
Chemical reaction controlled	$\tau^{-1}$ (s <sup>-1</sup> )	$5.39 \times 10^{-5}$ <sup>b)</sup> (1.000)	$5.37 \times 10^{-5}$ (0.919)	$6.54 \times 10^{-5}$ (0.999)	$3.02 \times 10^{-4}$ (0.710)
	<sup>a)</sup> $r_{\text{ini}}$ (nm)	46.5	unknown	46.5	unknown
	$k_b$ (nm/s)	0.157	–	0.191	–
Inter-diffusion controlled	$\tau^{-1}$ (s <sup>-1</sup> )	–	$1.72 \times 10^{-4}$ (0.889)	–	$7.43 \times 10^{-5}$ (0.991)

<sup>a</sup> half value of the average diameter of CoO at initial state.

<sup>b</sup> linear regression coefficient,  $R^2$



Schematic of the proposed reaction mechanism for cobalt nanoparticles formation in the reductive supercritical hydrothermal process.

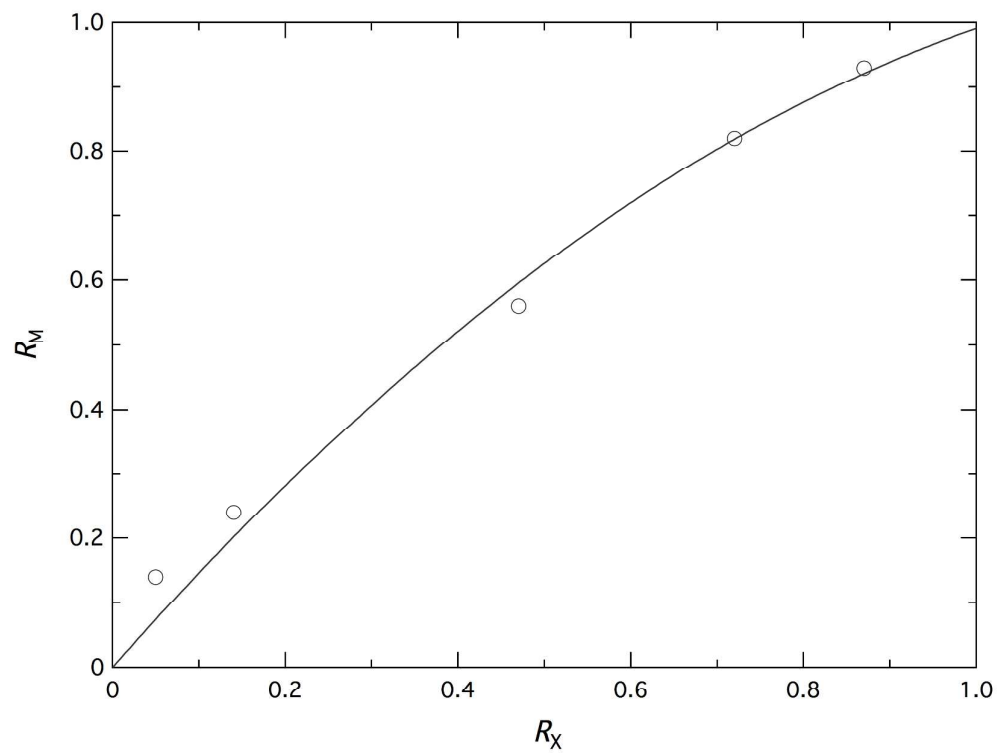


**Fig. 1** Standard curve for determining the molar ratio of the cobalt phase ( $R_M$ ) from the XRD peak area intensity ratio ( $R_X$ ).

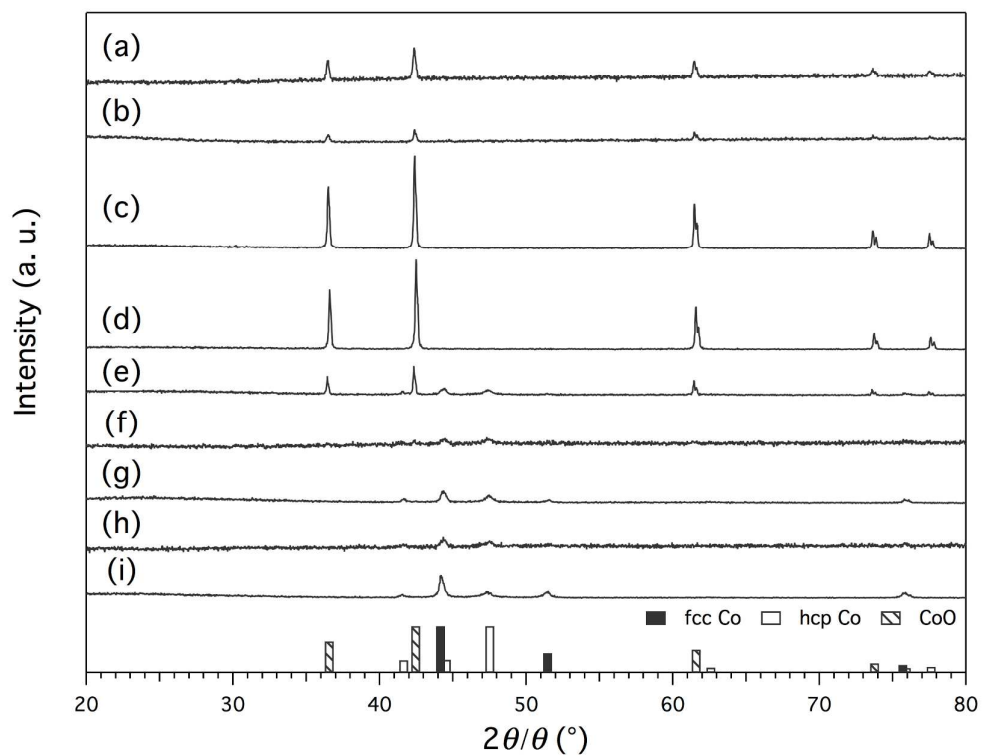


**Fig. 2** XRD peak patterns of the products synthesized at 340 °C. The loaded molar concentrations of formic acid were (a) 0.04, (b) 0.05, (c) 0.06, (d) 0.08, (e) 0.16, (f) 0.39, (g) 0.41, (h) 0.44 and (i) 0.53 M.

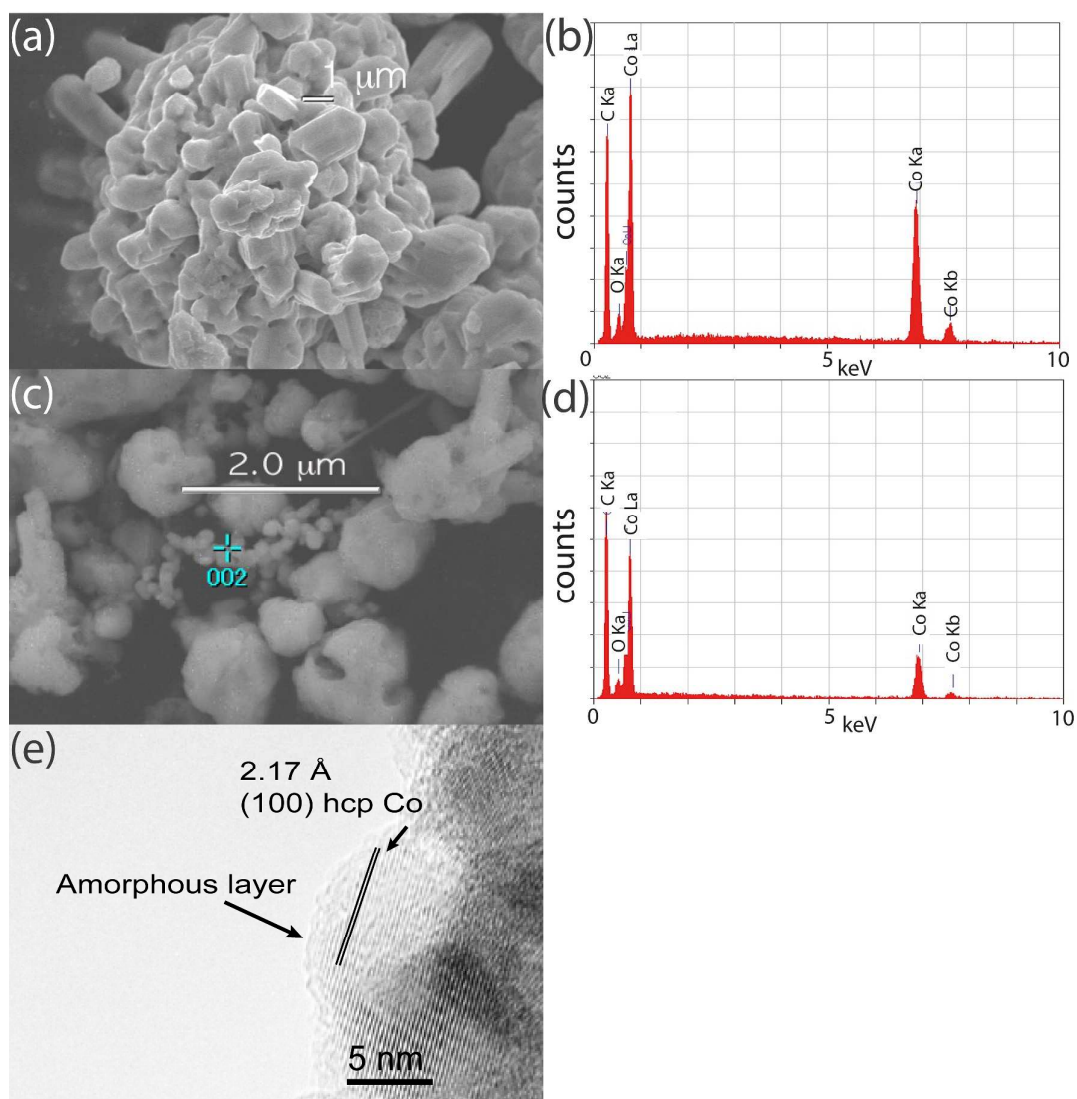


**Fig. 3** (a) SEM image of cobalt nanoparticles synthesized at 340 °C, (b) EDS spectrum of (a), (c) SEM image of cobalt nanoparticles synthesized at 380 °C, (d) EDS spectrum of (c) (particle indicated by the crosshair) and (e) high resolution TEM image of a part of the agglomerated particles in (c).

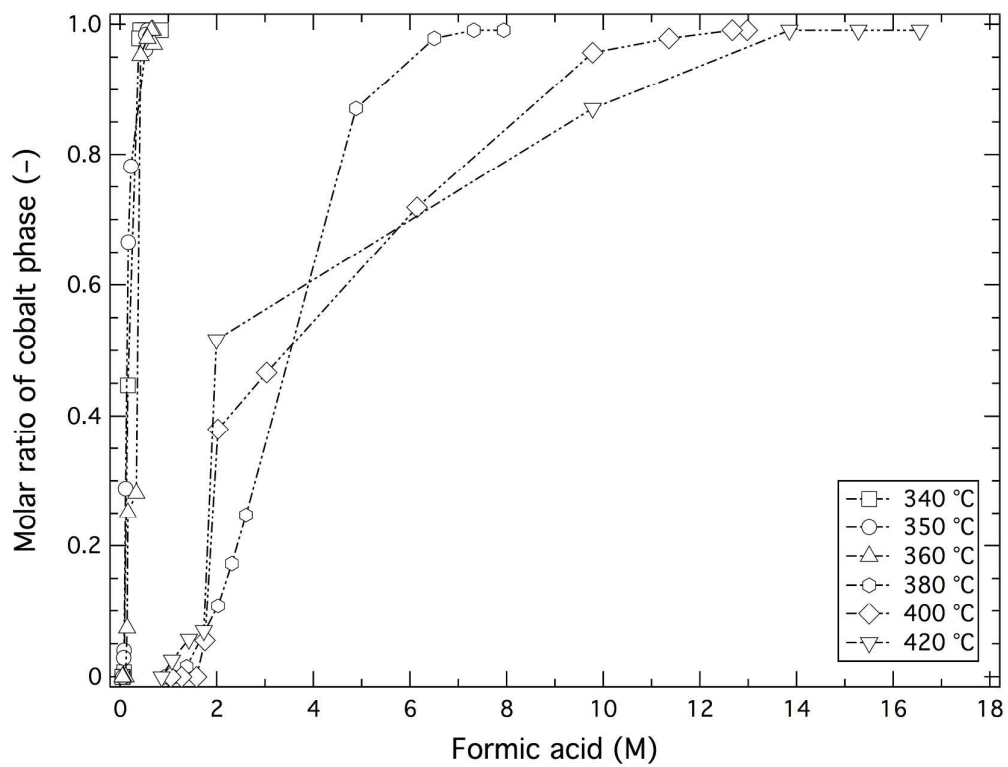


**Fig. 4** Molar ratios of cobalt phase in the products, as functions of loaded concentration of formic acid, under different isothermal conditions.

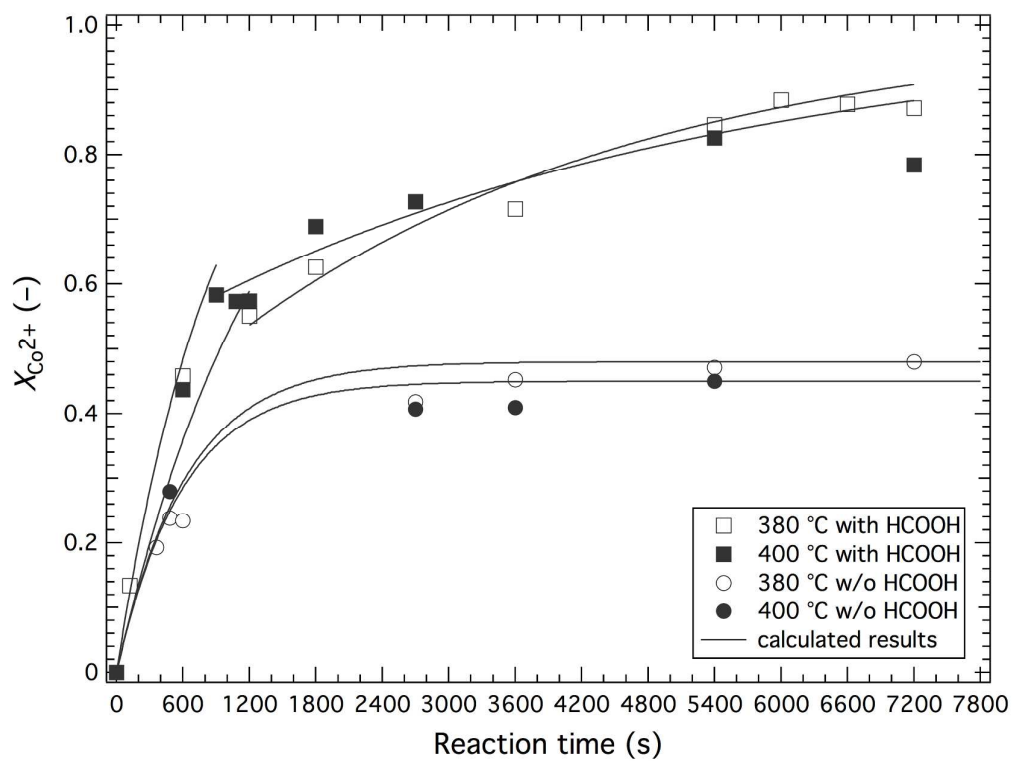


**Fig. 5** Conversion of cobalt ions,  $X_{Co^{2+}}$  as a function of reaction time.

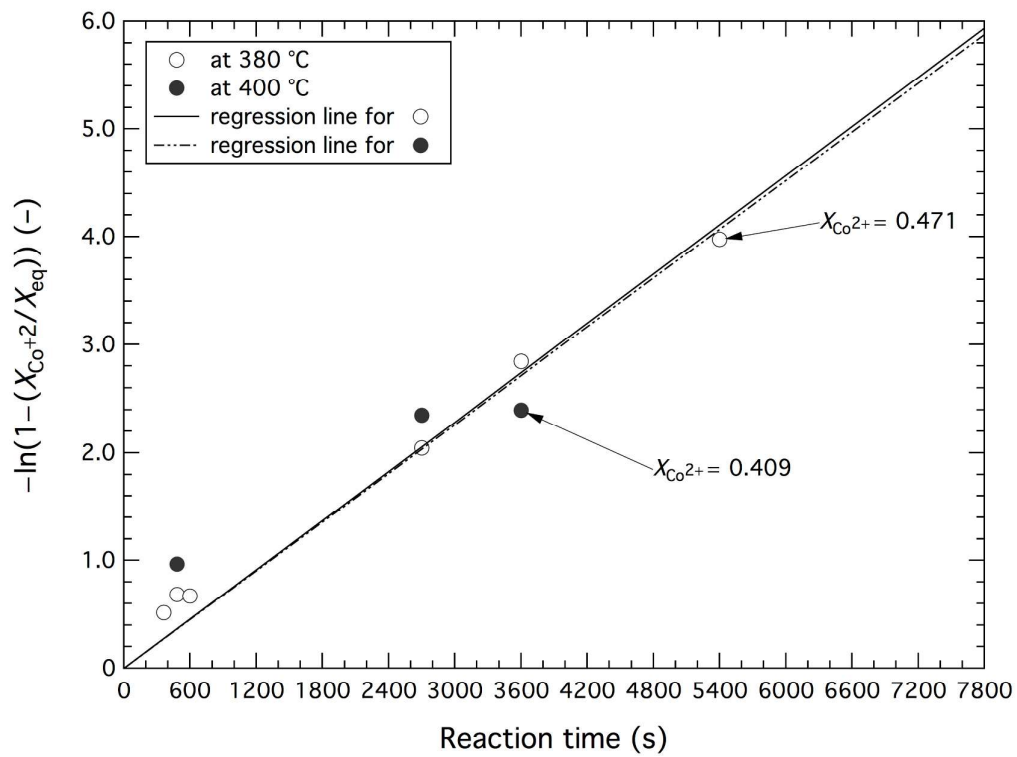


**Fig. 6** Plot of  $-\ln(1 - X_{\text{Co}^{2+}}/X_{\text{eq}})$  versus reaction time in the absence of formic acid (at 380 and 400 °C). The slope of the regression line is  $k_a/X_{\text{eq}}$ .

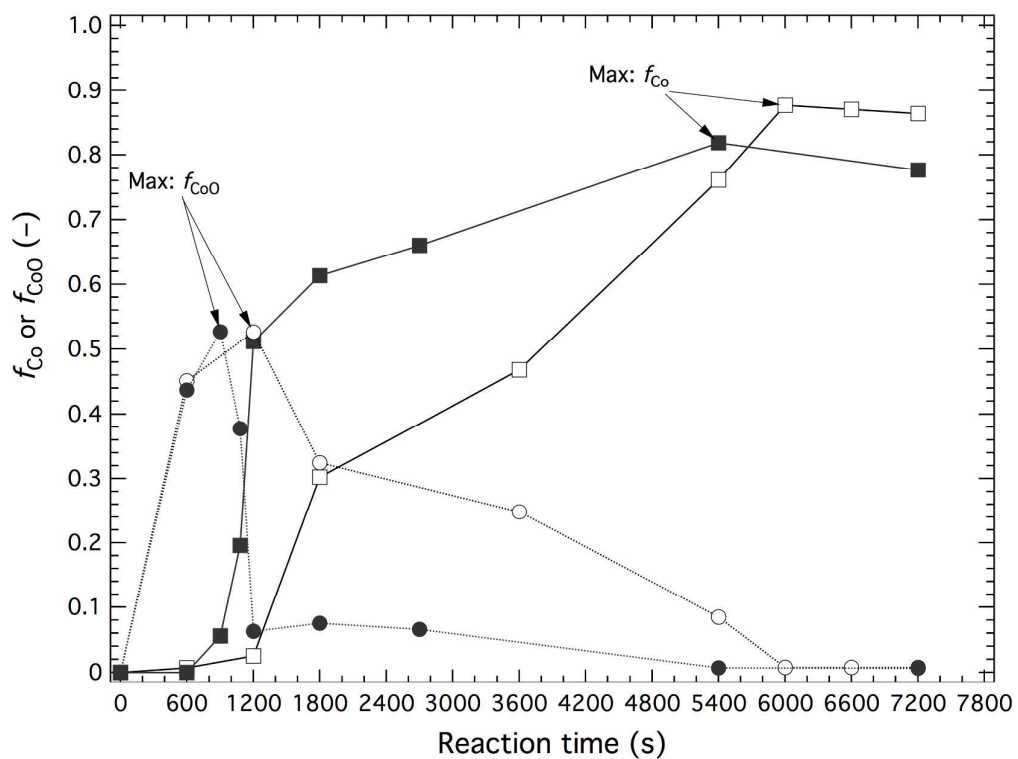


**Fig. 7** Reduction fraction  $f_{Co}$  and fraction of CoO  $f_{CoO}$  as function of reaction time.

Symbols represent: (□) $f_{Co}$  at 380 °C, (■) $f_{Co}$  at 400 °C, (○) $f_{CoO}$  at 380 °C, (●) $f_{CoO}$  at 400 °C and (—) and (---) are guide lines for the eyes.

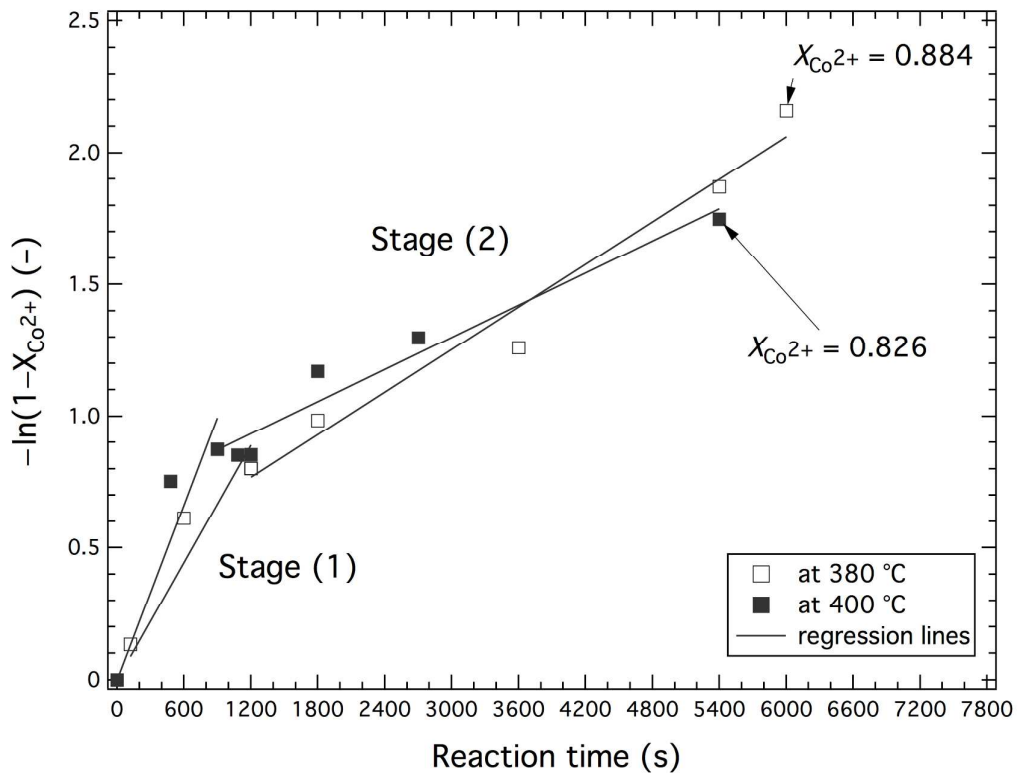


**Fig. 8** Plots of  $-\ln(1 - X_{\text{Co}^{2+}})$  versus the reaction time in the presence of formic acid.

The slopes of the regression lines yield the rate constants of reaction (a).

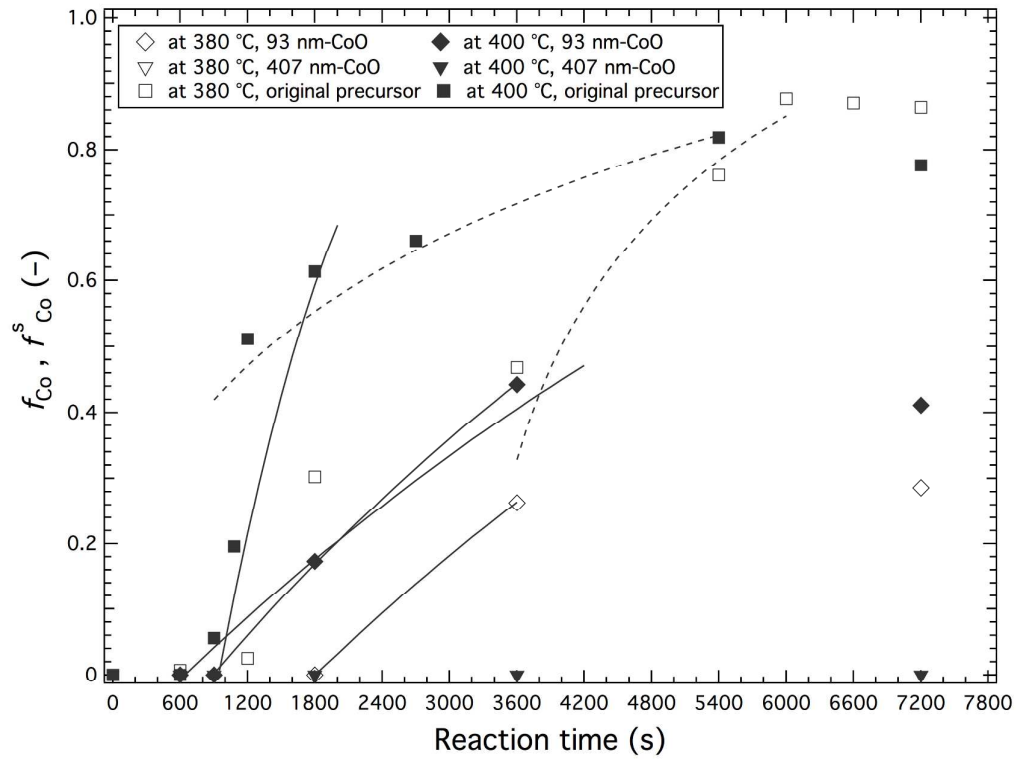


**Fig. 9** Reduction fractions  $f_{Co}$  &  $f_{Co}^s$  as function of reaction time. The calculated results are based on two shrinking core models: (—) indicates the chemical reaction controlled region, (---) indicates the inter-diffusion controlled region.

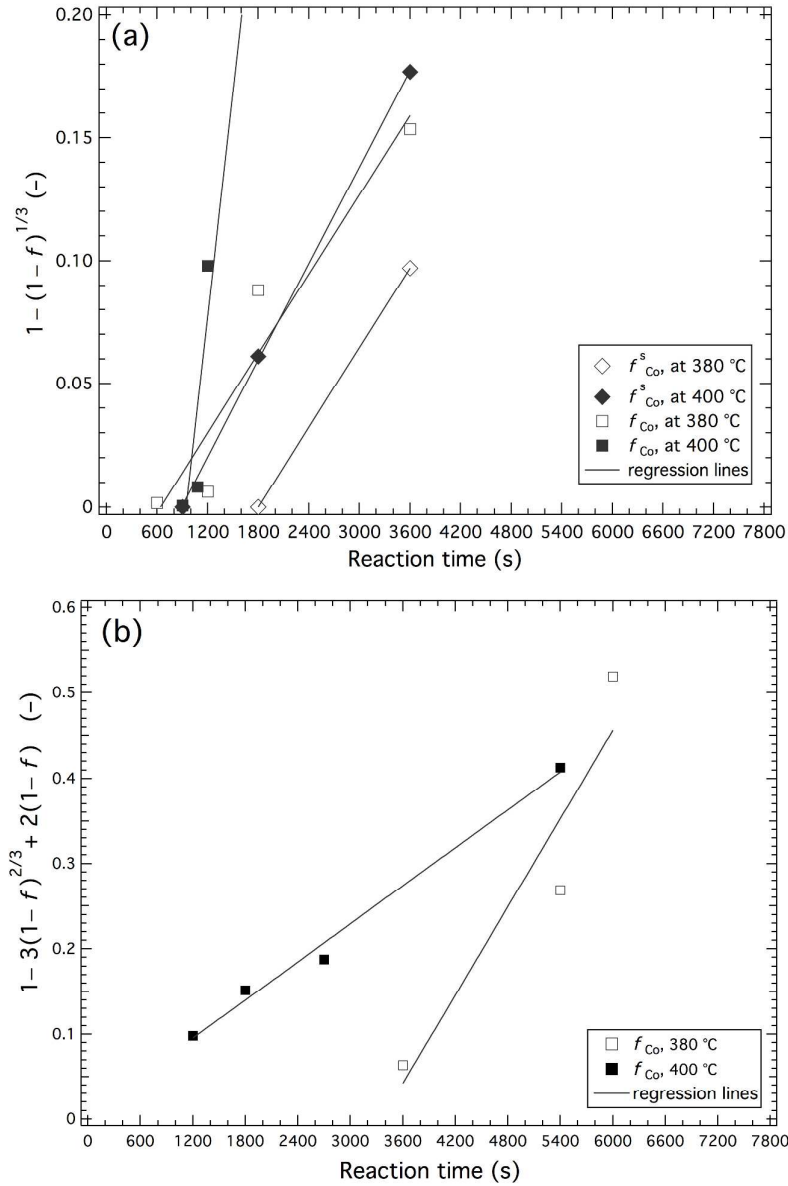


**Fig. 10** (a) Plot of  $1 - (1 - f)^{1/3}$  versus reaction time, assuming the parameters of the chemical reaction controlled shrinking core model, (b) plot of  $1 - 3(1 - f)^{2/3} + 2(1 - f)$  versus reaction time, assuming the parameters of the inter-diffusion controlled shrinking core model.

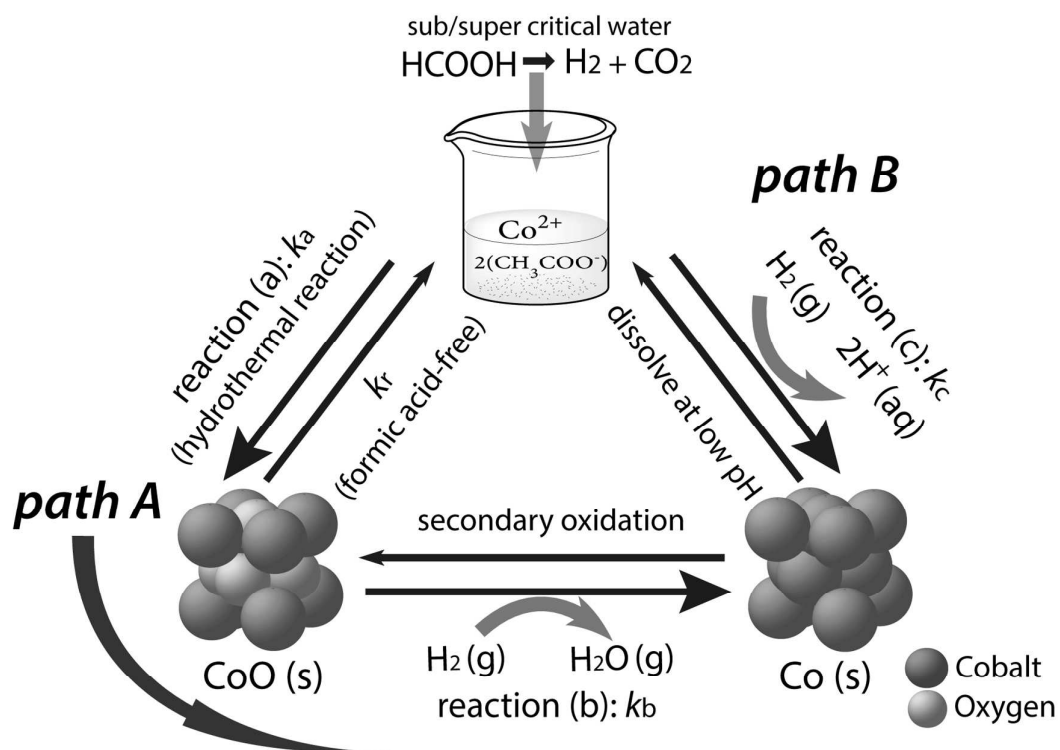


**Fig. 11** Schematic of the proposed reaction mechanism for cobalt nanoparticles formation in the reductive supercritical hydrothermal process.